CHEMISTRY OF MATERIALS

pubs.acs.org/cm Article

Tuning Ionic and Electronic Conductivities in the "Hollow" Perovskite {*en*}MAPbI$_3$

Alessandro Senocrate,[‖] Ioannis Spanopoulos,[‖] Nourdine Zibouche, Joachim Maier, M. Saiful Islam,* and Mercouri G. Kanatzidis*

Cite This: *Chem. Mater.* 2021, 33, 719−726

ABSTRACT: The recently developed family of 3D halide perovskites with general formula (A)$_{1-x}$(*en*)$_x$(M)$_{1-0.7x}$(I)$_{3-0.4x}$ (A = MA, FA; M = Pb^{2+}, Sn^{2+}; *en* = ethylenediammonium), often referred to as "hollow" perovskites, exhibits exceptional air stability and crystallizes in the high symmetry α phase at room temperature. These properties are counterintuitive, considering that these structures include the large divalent *en* cation charge-compensated by vacancies of Pb cations and I anions. Moreover, the understanding of their transport behavior is incomplete. To provide new insights into the ionic and electronic transport properties of these "hollow" perovskites, we performed DC polarization experiments and *ab initio* calculations on the {*en*}MAPbI$_3$ material. We observe large variations of ionic and electronic conductivities with *en* concentration, which can be explained by charge and site arguments in conjunction with trapping effects. The latter is reflected by the increase of the activation energies for iodide ion transport with higher *en* content that we observe from both experimental and computational results. The connection between these transport phenomena and the stability of "hollow" perovskite materials and devices is discussed.

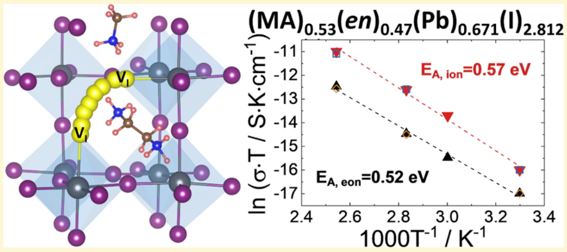

1. INTRODUCTION

Organic−inorganic (hybrid) halide perovskites are three-dimensional compounds with general formula AMX$_3$ (A = methylammonium, MA, formamidinium, FA, and Cs; M = divalent metal, X = Cl, Br, I).[1,2] The systems in which the metal is Pb and Sn are particularly important due to their applications in a wide variety of optoelectronic devices with exceptional performance.[3−6] In particular, their utilization as light harvesters in solar cell devices yielding competitive performance (power conversion efficiency values up to 25.5%)[7] has attracted immense scientific interest.[8−10] The higher the crystal symmetry, the smaller the deviation of the Pb−I−Pb bonds from 180°; this gives rise to maximum orbital overlap among Pb and I atoms and yields lower carrier effective masses.[11] This trait determines many optoelectronic properties of this family of materials, such as light absorption coefficients[12] and carrier lifetimes.[13−15]

Unfortunately, the majority of hybrid halide perovskites with band gaps in the optimum range for single-junction solar cells,[16,17] such as α-FAPbI$_3$ (1.40−1.44 eV)[18,19] and β-MAPbI$_3$ (1.51−1.55 eV),[12,19,20] are not stable in their undistorted cubic α phases at room temperature and can also exhibit instabilities arising from ion migration in the crystal structure.[21] Owing to this, a common strategy to stabilize the cubic phases at room temperature is the use of a mixture of A site cations (MA, FA, Cs)[22] as well as of X site anions (I, Br, Cl)[23,24] in the same compound. However, some of these types of mixed-anion perovskites undergo halide segregation upon illumination,[25−28] implying an enormous leeway for ion migration.[29]

Ion migration enabled by point defects may be an inherent problem in halide perovskites and ultimately may well prove to be the Achilles' heel of these systems. On the other hand, forced to live with such intrinsic defects, achieving control over ion migration becomes of utmost importance. As such, the understanding and tuning of ion migration are presently under intense investigation in this class of versatile materials.[30−36]

Recently, we have developed a new family of so-called "hollow" perovskites, with general formula (A)$_{1-x}$(*en*)$_x$(M)$_{1-0.7x}$(I)$_{3-0.4x}$ (A = MA, FA; M = Pb^{2+}, Sn^{2+}; *en* = ethylenediammonium) which seem more resistant to such ion migration.[19] They are considered a special kind of three-dimensional (3D) halide perovskites that exhibit significantly higher stability than the conventional 3D perovskites. The ethylenediammonium cation (*en*) can be incorporated into the 3D structure, even though according to the Goldschmidt tolerance factor criterion, this cation should be too large to fit in the A cage.[37,38] The structure is able to accommodate these

Received: October 23, 2020
Revised: December 21, 2020
Published: January 7, 2021

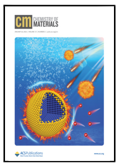

https://dx.doi.org/10.1021/acs.chemmater.0c04139

larger *en* cations by creating randomly dispersed pairs consisting of Pb or Sn cation vacancies and charge-compensating iodide ion vacancies in the inorganic network, which provide the required additional space. This was verified by a wide range of characterization techniques, such as single crystal and powder X-ray diffraction (XRD) measurements, which confirmed that the synthesized materials are indeed 3D perovskites.[19] Proton nuclear magnetic resonance spectroscopy (^{1}H NMR) measurements demonstrated that *en* is effectively incorporated into the crystal lattice. Crystal density measurements established that there is a marked decrease in mass density with an increasing amount of *en*, consistent with the presence of vacancies of the heavy Pb cations and I anions in the structure. This is further supported by electron dispersive spectroscopy (EDS) measurements finding a Pb/I ratio of 1:4 (as opposed to 1:3 in the non-hollow perovskites).[19]

Interestingly, this new structural "hollow" motif allows the fine-tuning of both absorption and emission spectra due to the occurrence of a blue shift with increasing amount of *en*.[19,38] DFT calculations have shed light on this phenomenon, ascribing it to the reduction of the number of M−I fragments, whose orbitals constitute the valence and conduction bands.[19,39] This narrows the widths of the electronic bands, increasing the bandgap proportionally to the inclusion of *en* in the lattice. Notably, this can be attained without reducing the dimensionality from 3D to 2D. Another prominent trait of this class of materials is their record air stability, which concerns both Pb^{2+} and Sn^{2+} perovskites. In particular, it is possible to stabilize the cubic α-$MAPbI_3$ phase at room temperature for almost a year (above 10% *en* inclusion). For the Sn-based analogues, there is a gradual increase in the air stability of the α-$MASnI_3$ phase by 2 orders of magnitude (16 days in air for the 40% *en*-based sample) compared to the pristine material, which is stable in air for around 10 min depending on humidity.[19] We took advantage of these favorable characteristics and assembled solar cells employing "hollow" perovskites, obtaining a very high and stable PCE value of 7% for a fully Sn-based perovskite solar cell, demonstrating the applicability of this novel class of semiconductors.[39]

Although the "hollow" perovskites exhibit higher stabilities, their ionic and electronic conductivities are poorly understood and as such deserve to be investigated in more detail. In this work, we combine experimental and simulation techniques to study, for the first time, the effect of *en* concentration on iodide ion transport in the {*en*}$MAPbI_3$ "hollow" perovskites. Ionic and electronic conductivity is examined through DC polarization measurements as a function of temperature, and *ab initio* modeling is used to probe the atomic-scale migration paths and trends in activation energies. When *en* is incorporated into the structure, the experimentally observed ion conductivity is initially slightly enhanced with respect to the *en*-free material but then decreases significantly on further increase of the *en* content, which is confirmed by the trends in computed activation energies for iodide ion migration. These measurements also show a substantial decrease in the electronic conductivity which, as the slowest contribution, is decisive for the chemical diffusion coefficient, at least in the dark.

2. RESULTS AND DISCUSSION

2.1. Structural Characterization. High-quality single crystals were synthesized according to previously published procedures.[19] The corresponding materials were characterized using PXRD measurements (Figure 1), as described in the Supporting Information. The incorporation of *en* into the crystal lattice gives rise to a β (tetragonal $I4/mcm$) to α (cubic Pm-$3m$) phase transformation above 10% *en* loading, while there is a gradual increase of the unit cell volume with increasing *en* amount, demonstrated by the shift of the diffraction pattern to lower 2θ values. Both these attributes represent signature characteristics of the 3D "hollow" perovskites. The phase transition is evident by the disappearance of the diffraction peaks at 2θ = 23.39° (211), 30.80° (213), and 42.59° (411) for samples with 10, 34, and 47% *en*. In order to validate and determine the amount of *en* that is actually incorporated into the structure, ^{1}H NMR measurements were carried out by dissolving the dried single crystals into a deuterated solvent (Supporting Information, Figures S1−S4). The quantification is based on the methyl ($-CH_3$, δ = 2.38 ppm) protons of the methylammonium cation *versus* the methylene ($-CH_2-$, δ = 3.02 ppm) protons of the ethylenediammonium cations. The ratio among the protons of the *en* cation is 4:6, indicating the double protonation of *en*. For simplicity purposes, instead of the general formula $(MA)_{1-x}(en)_x(Pb)_{1-0.7x}(I)_{3-0.4x}$, the following notation %{*en*}-$MAPbI_3$ will be utilized throughout the article to describe the "hollow" perovskites.

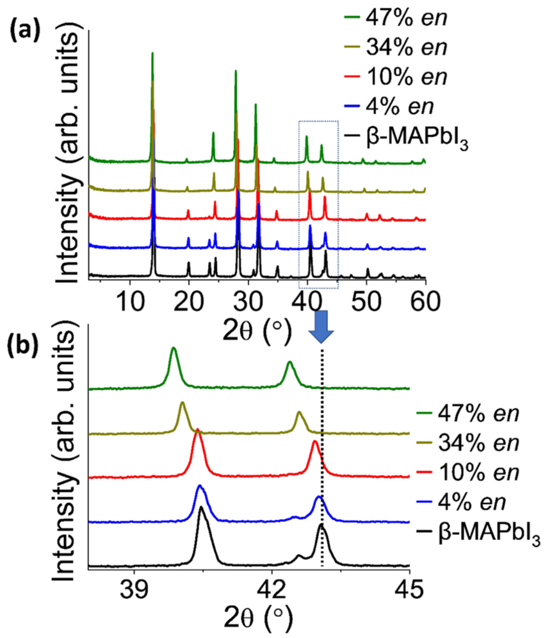

Figure 1. (a) Comparison of experimental PXRD patterns of the $(MA)_{1-x}(en)_x(Pb)_{1-0.7x}(I)_{3-0.4x}$ compounds with increasing amount of *en*. The 4% *en* "hollow" perovskite is isostructural to the pristine β phase $MAPbI_3$, while the rest of the "hollow" materials for x values up to 47% are isostructural to the pristine α phase $MAPbI_3$. (b) Highlighted area is enlarged to demonstrate the shift of the diffraction peaks to lower 2θ values (signaling a unit cell expansion) and phase transformation from β to α. The vertical dotted line is a guide for the eye.

2.2. Measurements of Conductivity *Versus en* Concentration. Figure 2 shows the results of DC polarization measurements carried out on {*en*}$MAPbI_3$ samples with different *en* concentrations. The measured voltage response to the galvanostatic stimulus is evaluated as follows: the initial jump after switching the current on, and equivalently the drop

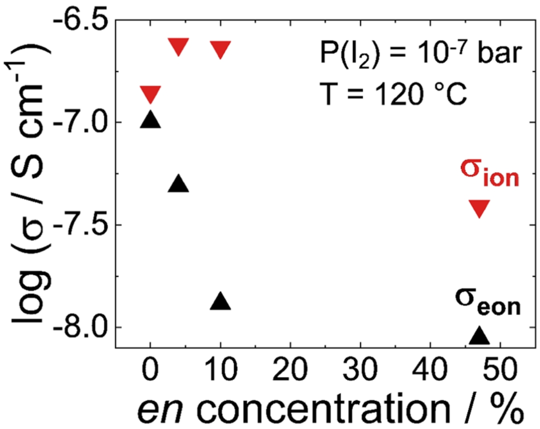

Figure 2. Ionic and electronic contributions to the conductivity of $MAPbI_3$ samples with different amounts of ethylenediammonium (*en*). The values are extracted from DC polarization measurements performed at 120 °C in the dark, under a constant iodine partial pressure of 10^{-7} bar (carrier gas = Ar).

after switching off, is attributed to the motion of both ions and electrons, while the steady state delivers solely the electronic contribution. The time dependence of the polarization is caused by the build-up of stoichiometric gradients and characterized by the chemical diffusion coefficient (a more detailed treatment is given in the Supporting Information, Section S4, while a full analysis is given elsewhere).[40,41] This presupposes the absence of significant electronic contributions from internal interfaces, an assumption supported by impedance spectroscopy.

The analysis reveals a predominant ionic conductivity that we attribute to iodide vacancies based on evidence from our previous experimental and computational studies[30,35,36] and on the simulation results discussed below. The electronic contribution is ascribed to holes, as shown by the enhancement of electronic conductivity upon increasing iodide partial pressure (see the Supporting Information, Figure S5). The dependence of the ionic conductivity on the *en* concentration shows an initial increase, followed by a marked decrease at higher *en* contents. As noted, previous structural characterization[19] indicates that the doubly charged *en* cation not only substitutes the A-site MA^+ cation but also requires the neighboring Pb^{2+}-site to be vacant, giving rise to an effectively negatively charged center (en^{2+} substituting both MA^+ and Pb^{2+}). This effective negative charge is compensated by an increase in the concentration of iodide vacancies, which are effectively positively charged. The significant decrease on higher *en* doping is therefore a characteristic feature of trapping (*e.g.*, acceptor dopant-anion vacancy interactions) or of more complex deviations from ideality (including variations of migration energies in the presence of high defect concentrations). This variation is in agreement with a substantial acceptor doping, which increases the concentration of positively charged carriers (iodide vacancies).

Charge carrier−dopant interaction can also explain the observed behavior of the electronic conductivity (σ_{eon}). The fact that we see already a strong decrease in the electronic conductivity at 4% *en* content points toward a greater sensitivity of σ_{eon} with respect to non-idealities. This behavior is independently reflected in the finding that even such low *en* contents can induce band-gap variations.[4] It should be noted that the absolute conductivity of nominally pure $MAPbI_3$ is probably the least defined value, as it can be influenced by unknown background impurities. As such, we expect the initial increase to vary with preparation conditions, but the qualitative features to still be meaningful.

For the discussion of the activation energies, it is important to recall the details of sample conditioning. A measurement under a given iodine partial pressure could not be performed as the equilibration times for low temperatures are much too long. Hence, the procedure described in a previous work on defect chemistry was followed.[42] The sample was equilibrated at a relatively high temperature (120 °C) under constant iodine partial pressure, where the equilibration still takes a long time but can be established. Then, the temperature dependence was rapidly measured. Thus, as far as the interaction with the gas phase is concerned, the samples can be considered to be frozen at lower temperatures. Hence, the results refer to a constant sample stoichiometry (no variations of defect concentration upon heating), and temperature effects include effects on the migration of charge carriers (variation of migration energies, *i.e.*, of the hopping barriers) and association energies. For the conductivity measurements, it helps that the relaxation times for the polarization are typically shorter than the equilibration with the gas phase (a point that will be taken up below) but still so long that extrapolation is typically necessary to determine the partial conductivities (see *e.g.*, ref 43). As shown in Figure 3, the ionic activation energy increases modestly from 0.26 to 0.34 eV when *en*-doping of 4% is employed but almost doubles (0.57 eV) when reaching 47% *en* content. The same trend is observed by ab initio calculations and discussed in the next section. In the first approximation, 0.26 eV can be assigned to the migration energy of iodide vacancies (as stated above, the experiments refer to constant defect concentrations), while the excess values can be ascribed to trapping and non-idealities. Concerning the electronic conduction, we expect the temperature dependence of the electronic mobility to be negligible[44] compared to the formation energy of the electronic defects (including trapping

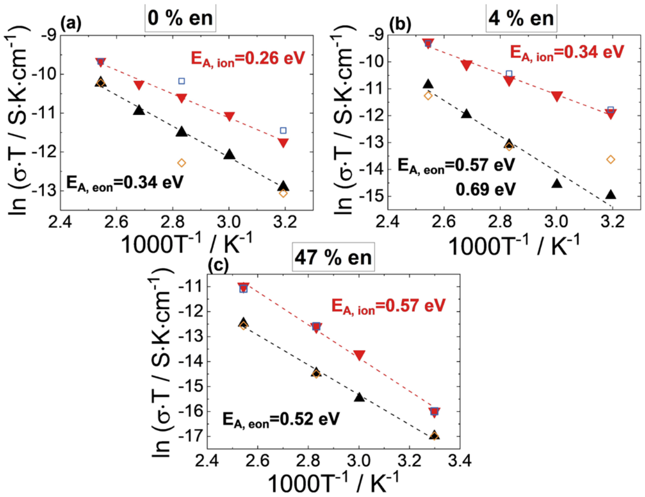

Figure 3. Arrhenius conductivity plots and activation energies for different *en* contents in %{*en*}$MAPbI_3$. Closed symbols represent data measured from low to high temperature, while open symbols show data collected from high back to low temperature to check reversibility. (a) 0% *en*, (b) 4% *en*, and (c) 47% *en*. The trends are extracted from DC galvanostatic polarization measurements performed as a function of temperature.

effects); therefore, we attribute the observed temperature variations to the latter.

A relevant property is kinetic stability with respect to iodine loss;[45] let us consider as an example iodine loss from the lattice due to heating. As detailed previously,[43,46] iodine first diffuses from the bulk of the material to the surface (ambipolar bulk transport with iodide ions and electronic species as charge carriers), where a sequence of surface reaction steps have to be undergone before it is released into the gas phase as I_2. Improving the kinetic stability of a material can thus be achieved by influencing the bulk transport step and/or the surface step. Considering the bulk transport process, the key parameter is the respective chemical diffusion coefficient (D^{δ}), here represented by the chemical diffusion coefficient of iodine (see for details the Supporting Information, Section S4). The most favorable situation would be a far-reaching absence of ion conductivity. These values indeed become significantly lower at high *en* concentration but are perceptible and still higher than the electronic conductivities. The fact that in the dark, the electronic conductivity, and certainly the electronic carrier concentration, is lower than the ionic counterpart makes D^{δ} electronically limited. For such a situation we have the following:[43]

$$D^{\delta} = D_{\text{eon}}\,\chi_{\text{eon}}$$

where D_{eon} is the diffusion coefficient of the electronic species and χ_{eon} is the trapping factor. The strong decrease of D_{eon} with *en* concentration (Figure 2) lowers D^{δ} significantly and should thus increase the kinetic stability. The trapping factor (χ_{eon}) depresses D^{δ} even below the value determined by D_{eon} alone. A treatment under high iodine partial pressure is helpful to increase σ_{eon}, but it would also enhance D^{δ}.

While D^{δ} characterizes the transient of a bulk-diffusion controlled decomposition reaction, the steady-state rate is characterized by σ^{δ} (proportional to the harmonic mean of ionic and electronic conductivities) and hence also given by the slowest species. All these results refer to the dark situation. Owing to the high *en* doping concentrations, and to the experience with $MAPbI_3$, one does not expect the chemical relaxation times to become so large under illumination that they could explain the kinetic stability.[47] Rather, neither the absolute values of the relaxation times of the DC polarization nor the variation on the *en* content can explain the remarkable stability of "hollow" perovskites (DC polarization time scales are on the order of 3 min for 0% and 15 min for 4% *en*, as shown in the Supporting Information, Figure S6). Instead, the much higher relaxation times of the observed iodine gas/solid exchange are revealing. Here, absolute values and the magnitude of the variation (equilibration time scales $\tau \sim 8$ h for 0% and $\tau \sim 200$ h for 4% *en* at 80 °C, shown in Figure 4) are closer to the reported stability time windows. As mentioned above and detailed previously,[43,46] the difference between the two experiments is that the iodine exchange also includes surface reaction steps (charge transfer, ionization or deionization, adsorption or desorption).

The occurrence that the surface reaction is much more sluggish than bulk diffusion at these low temperatures is not at all surprising and has been well established for various perovskite oxides such as $SrTiO_3$.[48,49] Note that varying the surface resistance or bulk chemical diffusion coefficients does not have an impact on the thermodynamic stability of the materials, which may present an appreciable driving force toward decomposition. Nevertheless, improving kinetic stability may suffice in yielding important improvements toward the applications of these "hollow" perovskite materials. The detailed mechanism of the influence of *en doping* on the surface kinetics is beyond the scope of this study and warrants future investigation.

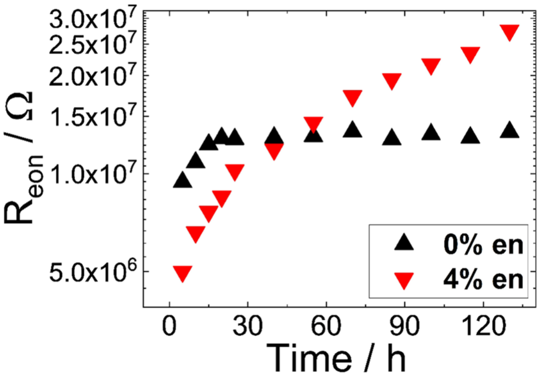

Figure 4. Variation of the electronic conductivity (saturation voltage of the DC polarization curve) as a function of time, recorded at 80 °C after varying the atmosphere over the samples from Ar containing $P(I_2) = 10^{-7}$ bar to pure Ar. Undoped $MAPbI_3$ samples equilibrate much faster.

2.3. Atomistic Migration Pathways. As noted above, the macroscopic conductivity measurements find an increase in the ionic activation energy with increasing *en* content. To provide further insights at the atomic level, we have performed *ab initio* DFT simulations on the pathways and relative activation energies for iodide ion migration in $\{en\}MAPbI_3$, extending our previous ion transport studies of halide perovskites.[30,36] (Details on the computational techniques, which have been used in recent studies on perovskites[22,36,50−53] are provided in the Supporting Information, Section S1). With regard to the structure of the doped $MAPbI_3$ system, the simulations support the structural characterization in which the divalent *en* cation substitutes both MA^+ and Pb^{2+}, with charge-compensation by iodide vacancies. Such defect chemistry would support iodide vacancy-mediated ionic conductivity. Because of symmetry and supercell size considerations for these complex "hollow" structures, we simulated two *en* contents of 6.25 and 37.5%.

To investigate the impact of increasing the *en*-content, we considered six possible pathways for iodide vacancy migration between neighboring sites with very similar diffusion lengths and local environments of the two *en* concentrations, shown in Figure 5. These migration pathways (indicated by arrows) share two final iodine vacancy positions, $V_I(A)$ and $V_I(B)$, with the initial iodide vacancy positions assigned as $V_I(1)$ to $V_I(5)$. These nonequivalent vacancy positions were chosen from the local octahedron environment of the Pb vacancy and the adjacent PbI_6 octahedron below. Although we recognize that other paths are possible, the number of paths considered near the *en* cation allows us to probe trends in migration activation energies for the two *en* concentrations, which is the main focus here.

Energy profiles for these pathways were mapped out between adjacent sites to derive activation energies, and particular care was taken to ensure full convergence (with the values listed in Table S1). For long-range ion migration in the two *en* contents considered, we extracted the mean activation energy of 0.56 eV for the migration pathways in the 6.25% *en* material, whereas in the 37.5% *en* material, the mean activation

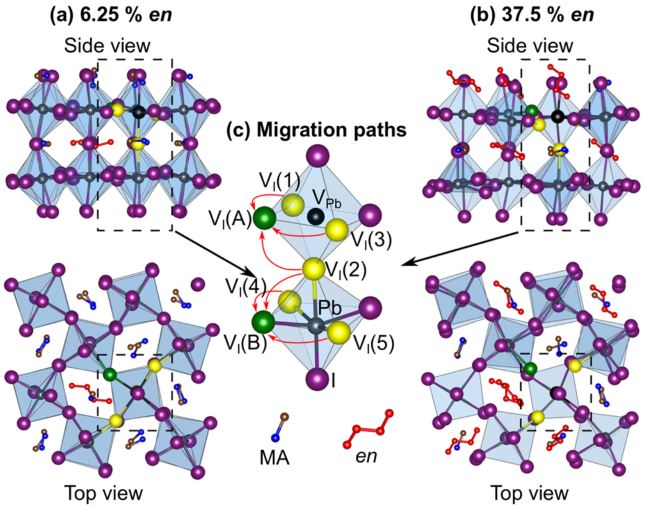

Figure 5. Simulated crystal structures and ion migration paths of *en* $MAPbI_3$. (a) 6.25% *en* (b) and 37.5% *en* content. For clarity, the hydrogen atoms are omitted, and the C and N atoms of the *en* cations are highlighted in red. (c) Iodide ion migration pathways are indicated by the arrows between the initial nonequivalent iodide vacancy positions (yellow) marked as $V_I(1)$ to $V_I(5)$, and the final iodine vacancy positions (green), $V_I(A)$ and $V_I(B)$.

energy has a higher value of 0.69 eV. Our focus here is on the atomistic pathways and on the trends in energies; indeed, these results find qualitative agreement with the experimental conductivity data in showing increasing ionic activation energy with increasing *en* content. Overall, these ionic activation energies are slightly higher than the experimental values, which can be attributed to the complex anisotropy and the structural distortion in these *en*-containing systems.

The *ab initio* simulations also provide useful structural information. The presence of the much larger *en* cation and compensating vacancies can cause an increase in the volume of the Pb/I cage and distortion of the local inorganic framework, as well as dopant-vacancy trapping effects. Our simulation analysis of the local structure around the *en* cation indicates significant local ion displacements leading to an increase of ~0.6 and ~0.25 Å of the Pb−Pb and I−I distances, respectively, within the Pb/I cage. These structural changes result in higher activation energies for iodide ion migration in the highly *en*-substituted perovskite. It is worth noting that such atomic-scale mechanistic and local structural features are difficult to extract from experiments alone, and one of the aims of this study is to stimulate further work in this area.

3. CONCLUSIONS

Our combined experimental-computational study has provided new insights into the transport properties of the ethylenediammonium (*en*)-based 3D "hollow" perovskite $(MA)_{1-x}(en)_x(Pb)_{1-0.7x}(I)_{3-0.4x}$ in which we observe large variations of ionic and electronic conductivities with *en* concentration. The DC polarization measurements show that with increasing *en* content there is a small initial increase in ionic conductivity and then a substantial decrease for higher *en* contents. This can be attributed to the expected doping behavior in which the divalent *en* cation substitutes both MA^+ and Pb^{2+}, with charge-compensation by iodide vacancies, in conjunction with trapping interactions of the highly concentrated *en* dopants with the charge carriers. The latter is reflected by the increase of the activation energies for iodide ion migration with higher *en* content that we observe from both experimental data and *ab initio* simulations. In contrast, the electronic conductivities feel the non-idealities already at lower *en* concentrations and decrease monotonically. Our significant finding that, in the dark, electronic contributions to the conductivity are always smaller than the ionic contributions indicates that they determine the chemical bulk relaxation times under these conditions.

This combined study enhances our fundamental understanding of transport phenomena in the $\{en\}MAPbI_3$ "hollow" perovskite and shows the strong influence of *en* substitution on both ionic and electronic conductivities. As well as the effect of these bulk parameters, the transient experiments point toward an important role of surface kinetics in the stability of "hollow" perovskite-based solar cells. We also expect these insights to be applicable to the corresponding Sn-based hollow perovskites.

4. EXPERIMENTAL AND METHODS SECTION

4.1. Starting Materials and Synthesis. All starting materials for synthesis were purchased commercially and were used without further purification. Lead(II) acetate trihydrate puriss. p.a., ACS, 99.5−102.0%, ACS, ≥98%, Methylamine hydrochloride ≥98%, hypophosphorous acid solution 50 wt % in H_2O, hydriodic acid 57 wt % in H_2O, distilled, stabilized, 99.95%, Ethylenediamine ReagentPlus, ≥99%, and dimethyl sulfoxide-d_6 99.9 atom %*D* were purchased from Aldrich. All materials were synthesized according to published procedures.[19] The crystals were filtered under vacuum and dried at 120 °C for 10 h.

4.2. PXRD and ^{1}H NMR Measurements. Powder X-ray diffraction patterns were collected on a Rigaku Miniflex system (Cu Kα radiation) operated at 40 kV and 15 mA. The typical scan rate was 20 s/step with a step size of 0.02 deg. ^{1}H NMR spectra were recorded on 600 MHz Bruker, A600 spectrometer. All samples were prepared by dissolving a small portion of the dried solids (~10 mg) in a DMSO-d_6 solution (0.5 mL).

4.3. Sample Preparation for Electrical Measurements. Samples for electrical measurements were prepared by cold pressing powders into pellets of 5 mm diameter. During the pressing step, carbon electrodes cut from carbon felt were added to obtain a symmetric assembly ready to be measured. In a typical DC polarization measurement, the sample is inserted in a cell where temperature and atmosphere composition are carefully controlled and monitored. Typically, samples are exposed to an Ar atmosphere containing a moderate but constant I_2 partial pressure. The latter is obtained by flowing the gas through a gas wash bottle containing solid I_2, which is immersed in a thermostat set at low temperatures. The equilibrium pressure of iodine at the thermostat temperature is considered to represent the iodine partial pressure within the measurement cell.

4.4. DC Polarization Measurements. In a typical experiment, very small (*ca.* 1−10 nA) currents are applied to the samples while the voltage response is recorded. This is achieved by employing a high impedance source/meter (Keithley model 2634B). All measurements are performed in the dark.

4.5. Activation Energy Measurements. The samples are initially equilibrated at 120 °C under $P(I_2) = 10^{-7}$ bar until their electrical properties stop changing significantly (approximately 72 h). Then, the samples are cooled and the electrical properties are rapidly measured (within a few hours at each temperature). To check reversibility, the samples are heated again to 120 °C and the electrical property reassessed during the heating ramp.

4.6. Equilibration Time Measurements. The variation upon changing the atmosphere over a sample was recorded through DC galvanostatic polarization measurements as a function of time. Typically, a polarization curve (requiring about 4 h) is collected with a time delay of 5−10 h.

4.7. Computer Simulations. DFT calculations[54] were carried out using the plane-wave pseudopotential method as implemented in the Quantum ESPRESSO package.[55,56] The Kohn−Sham wave-functions and energies are calculated with the PBE functional[57,58] and the Grimme dispersion correction DFT-D3[59] to account for the van der Waals terms. Ultrasoft pseudopotentials[60] are used to describe the core−valence interactions with plane-wave energy and charge density cutoffs of 40 Ry and 400 Ry, respectively. The structural relaxation is performed until the force on each atom is smaller than 0.01 eV/AÅ. The Brillouin zone integration was sampled following the Monkhorst−Pack scheme[61] with a k-points grid of 2 × 2 × 3. The structure model used for the simulations is a 2 × 2 × 1 supercell containing 16 MA-cations constructed from the tetragonal phase of $MAPbI_3$. The MA cations are then substituted by ethylenediammonium (*en*) cations, resulting in compositions with *en* ratios of 6.25 and 37.5%. Pb and I atoms were removed to ensure charge neutrality. The concentration of the compensating vacancies are one Pb/one I atoms and four Pb/two I atoms in the 6.25 and 37.5% compositions, respectively. The nudged elastic band (NEB) method is used for determining the migration pathway and the activation energy between two energetically stable points. Calculations with respect to the number of images for one migration path was carried out for 7, 9, and 11 NEB images, for which convergence is achieved with 9 images within an error of 0.03 eV. Therefore, for conclusive results a discretized migration path of 11 images was used throughout the study, where the intermediate images were obtained by linear interpolation. For a rigorous convergence on the highest saddle point, the climbing image method is also used. The activation energies were calculated as the difference between the maximum and minimum energies of the calculated NEB images.

In order to examine the sensitivity of the migration activation energies to the size of the supercell model and hence to the periodic boundary conditions, we have performed NEB calculations for the same migration path for the 6.25% composition using two different supercell sizes: (i) the same supercell size as above with 196 atoms and (ii) twice the supercell size of (i) in the *z* direction with 392 atoms. The calculated activation energies are 0.795 and 0.781 eV for the supercells (i) and (ii), respectively. The very small energy difference of 0.013 eV between the two supercells indicates that the calculated activation energies with the supercell model (i) used in our study have converged with respect to the system size.

■ ASSOCIATED CONTENT

Supporting Information

The Supporting Information is available free of charge at https://pubs.acs.org/doi/10.1021/acs.chemmater.0c04139.

Material characterization, ^1H NMR measurements, conductivity data, and DC polarization curves and time constants (PDF)

■ AUTHOR INFORMATION

Corresponding Authors

M. Saiful Islam − *Department of Chemistry, University of Bath, Bath BA2 7AY, U.K.;* orcid.org/0000-0003-3882-0285; Email: m.s.islam@bath.ac.uk

Mercouri G. Kanatzidis − *Department of Chemistry, Northwestern University, Evanston, Illinois 60208, United States;* orcid.org/0000-0003-2037-4168; Email: m-kanatzidis@northwestern.edu

Authors

Alessandro Senocrate − *Max Planck Institute for Solid State Research, Stuttgart 70569, Germany*

Ioannis Spanopoulos − *Department of Chemistry, Northwestern University, Evanston, Illinois 60208, United States;* orcid.org/0000-0003-0861-1407

Nourdine Zibouche − *Department of Chemistry, University of Bath, Bath BA2 7AY, U.K.*

Joachim Maier − *Max Planck Institute for Solid State Research, Stuttgart 70569, Germany*

Complete contact information is available at: https://pubs.acs.org/10.1021/acs.chemmater.0c04139

Author Contributions

[‖]A.S. and I.S. contributed equally to this work.

Notes

The authors declare no competing financial interest.

■ ACKNOWLEDGMENTS

M.G.K. acknowledges funding by U.S. DOE, Office of Science (grant SC0012541, sample synthesis, characterization). M.S.I. and N.Z. gratefully acknowledge an EPSRC Grant (EP/R020485/1) and the MCC/Archer supercomputing consortium (EP/L000202/1).

■ REFERENCES

(1) Stoumpos, C. C.; Kanatzidis, M. G. Halide Perovskites: Poor Man's High-Performance Semiconductors. *Adv. Mater.* **2016**, *28*, 5778−5793.

(2) Stoumpos, C. C.; Malliakas, C. D.; Kanatzidis, M. G. Semiconducting Tin and Lead Iodide Perovskites with Organic Cations: Phase Transitions, High Mobilities, and Near-Infrared Photoluminescent Properties. *Inorg. Chem.* **2013**, *52*, 9019−9038.

(3) Kim, Y. C.; Kim, K. H.; Son, D.-Y.; Jeong, D.-N.; Seo, J.-Y.; Choi, Y. S.; Han, I. T.; Lee, S. Y.; Park, N.-G. Printable organometallic perovskite enables large-area, low-dose X-ray imaging. *Nature* **2017**, *550*, 87−91.

(4) Christians, J. A.; Schulz, P.; Tinkham, J. S.; Schloemer, T. H.; Harvey, S. P.; Tremolet de Villers, B. J.; Sellinger, A.; Berry, J. J.; Luther, J. M. Tailored interfaces of unencapsulated perovskite solar cells for >1,000 hour operational stability. *Nat. Energy* **2018**, *3*, 68−74.

(5) Zhao, X.; Tan, Z.-K. Large-area near-infrared perovskite light-emitting diodes. *Nat. Photonics* **2020**, *14*, 215−218.

(6) Kim, H.; Roh, K.; Murphy, J. P.; Zhao, L.; Gunnarsson, W. B.; Longhi, E.; Barlow, S.; Marder, S. R.; Rand, B. P.; Giebink, N. C. Optically Pumped Lasing from Hybrid Perovskite Light-Emitting Diodes. *Adv. Opt. Mater.* **2020**, *8*, 1901297.

(7) National Renewable Energy Laboratory. Research Cell Record Efficiency Chart, 2020, https://www.nrel.gov/pv/cell-efficiency.html (accessed December 21, 2020).

(8) Yin, W.-J.; Shi, T.; Yan, Y. Unique Properties of Halide Perovskites as Possible Origins of the Superior Solar Cell Performance. *Adv. Mater.* **2014**, *26*, 4653−4658.

(9) Zheng, X.; Wu, C.; Jha, S. K.; Li, Z.; Zhu, K.; Priya, S. Improved Phase Stability of Formamidinium Lead Triiodide Perovskite by Strain Relaxation. *ACS Energy Lett.* **2016**, *1*, 1014−1020.

(10) Kim, S.; Eom, T.; Ha, Y.-S.; Hong, K.-H.; Kim, H. Thermodynamics of Multicomponent Perovskites: A Guide to Highly Efficient and Stable Solar Cell Materials. *Chem. Mater.* **2020**, *32*, 4265−4272.

(11) Yin, W.-J.; Yang, J.-H.; Kang, J.; Yan, Y.; Wei, S.-H. Halide perovskite materials for solar cells: a theoretical review. *J. Mater. Chem. A* **2015**, *3*, 8926−8942.

(12) Leguy, A. M. A.; Azarhoosh, P.; Alonso, M. I.; Campoy-Quiles, M.; Weber, O. J.; Yao, J.; Bryant, D.; Weller, M. T.; Nelson, J.; Walsh, A.; van Schilfgaarde, M.; Barnes, P. R. F. Experimental and theoretical optical properties of methylammonium lead halide perovskites. *Nanoscale* **2016**, *8*, 6317−6327.

(13) Lu, Y.-B.; Yang, H.; Cong, W.-Y.; Zhang, P.; Guo, H. Temperature dependence of the effective mass of the hybrid organic-

inorganic perovskites $CH_3NH_3PbI_3$. *Appl. Phys. Lett.* **2017**, *111*, 253902.

(14) Galkowski, K.; Mitioglu, A.; Miyata, A.; Plochocka, P.; Portugall, O.; Eperon, G. E.; Wang, J. T.-W.; Stergiopoulos, T.; Stranks, S. D.; Snaith, H. J.; Nicholas, R. J. Determination of the exciton binding energy and effective masses for methylammonium and formamidinium lead tri-halide perovskite semiconductors. *Energy Environ. Sci.* **2016**, *9*, 962−970.

(15) Huang, J.; Yuan, Y.; Shao, Y.; Yan, Y. Understanding the physical properties of hybrid perovskites for photovoltaic applications. *Nat. Rev. Mater.* **2017**, *2*, 17042.

(16) Henry, C. H. Limiting efficiencies of ideal single and multiple energy gap terrestrial solar cells. *J. Appl. Phys.* **1980**, *51*, 4494−4500.

(17) Shockley, W.; Queisser, H. J. Detailed Balance Limit of Efficiency of p-n Junction Solar Cells. *J. Appl. Phys.* **1961**, *32*, 510−519.

(18) Saidaminov, M. I.; Abdelhady, A. L.; Maculan, G.; Bakr, O. M. Retrograde solubility of formamidinium and methylammonium lead halide perovskites enabling rapid single crystal growth. *Chem. Commun.* **2015**, *51*, 17658−17661.

(19) Spanopoulos, I.; Ke, W.; Stoumpos, C. C.; Schueller, E. C.; Kontsevoi, O. Y.; Seshadri, R.; Kanatzidis, M. G. Unraveling the Chemical Nature of the 3D "Hollow" Hybrid Halide Perovskites. *J. Am. Chem. Soc.* **2018**, *140*, 5728−5742.

(20) Saidaminov, M. I.; Abdelhady, A. L.; Murali, B.; Alarousu, E.; Burlakov, V. M.; Peng, W.; Dursun, I.; Wang, L.; He, Y.; Maculan, G.; Goriely, A.; Wu, T.; Mohammed, O. F.; Bakr, O. M. High-quality bulk hybrid perovskite single crystals within minutes by inverse temperature crystallization. *Nat. Commun.* **2015**, *6*, 7586.

(21) Weber, O. J.; Ghosh, D.; Gaines, S.; Henry, P. F.; Walker, A. B.; Islam, M. S.; Weller, M. T. Phase Behavior and Polymorphism of Formamidinium Lead Iodide. *Chem. Mater.* **2018**, *30*, 3768−3778.

(22) Ghosh, D.; Smith, A. R.; Walker, A. B.; Islam, M. S. Mixed A-Cation Perovskites for Solar Cells: Atomic-Scale Insights Into Structural Distortion, Hydrogen Bonding, and Electronic Properties. *Chem. Mater.* **2018**, *30*, 5194−5204.

(23) Unger, E. L.; Bowring, A. R.; Tassone, C. J.; Pool, V. L.; Gold-Parker, A.; Cheacharoen, R.; Stone, K. H.; Hoke, E. T.; Toney, M. F.; McGehee, M. D. Chloride in Lead Chloride-Derived Organo-Metal Halides for Perovskite-Absorber Solar Cells. *Chem. Mater.* **2014**, *26*, 7158−7165.

(24) Kim, M.; Kim, G.-H.; Lee, T. K.; Choi, I. W.; Choi, H. W.; Jo, Y.; Yoon, Y. J.; Kim, J. W.; Lee, J.; Huh, D.; Lee, H.; Kwak, S. K.; Kim, J. Y.; Kim, D. S. Methylammonium Chloride Induces Intermediate Phase Stabilization for Efficient Perovskite Solar Cells. *Joule* **2019**, *3*, 2179−2192.

(25) Brennan, M. C.; Draguta, S.; Kamat, P. V.; Kuno, M. Light-Induced Anion Phase Segregation in Mixed Halide Perovskites. *ACS Energy Lett.* **2018**, *3*, 204−213.

(26) Hoke, E. T.; Slotcavage, D. J.; Dohner, E. R.; Bowring, A. R.; Karunadasa, H. I.; McGehee, M. D. Reversible photo-induced trap formation in mixed-halide hybrid perovskites for photovoltaics. *Chem. Sci.* **2015**, *6*, 613−617.

(27) McMeekin, D. P.; Sadoughi, G.; Rehman, W.; Eperon, G. E.; Saliba, M.; Hörantner, M. T.; Haghighirad, A.; Sakai, N.; Korte, L.; Rech, B.; Johnston, M. B.; Herz, L. M.; Snaith, H. J. A mixed-cation lead mixed-halide perovskite absorber for tandem solar cells. *Science* **2016**, *351*, 151−155.

(28) Chen, W.; Li, W.; Gan, Z.; Cheng, Y.-B.; Jia, B.; Wen, X. Long-Distance Ionic Diffusion in Cesium Lead Mixed Halide Perovskite Induced by Focused Illumination. *Chem. Mater.* **2019**, *31*, 9049−9056.

(29) Braly, I. L.; Stoddard, R. J.; Rajagopal, A.; Uhl, A. R.; Katahara, J. K.; Jen, A. K.-Y.; Hillhouse, H. W. Current-Induced Phase Segregation in Mixed Halide Hybrid Perovskites and its Impact on Two-Terminal Tandem Solar Cell Design. *ACS Energy Lett.* **2017**, *2*, 1841−1847.

(30) Eames, C.; Frost, J. M.; Barnes, P. R. F.; O'Regan, B. C.; Walsh, A.; Islam, M. S. Ionic transport in hybrid lead iodide perovskite solar cells. *Nat. Commun.* **2015**, *6*, 7487.

(31) Pockett, A.; Eperon, G. E.; Sakai, N.; Snaith, H. J.; Peter, L. M.; Cameron, P. J. Microseconds, milliseconds and seconds: deconvoluting the dynamic behaviour of planar perovskite solar cells. *Phys. Chem. Chem. Phys.* **2017**, *19*, 5959−5970.

(32) Meloni, S.; Moehl, T.; Tress, W.; Franckevičius, M.; Saliba, M.; Lee, Y. H.; Gao, P.; Nazeeruddin, M. K.; Zakeeruddin, S. M.; Rothlisberger, U.; Graetzel, M. Ionic polarization-induced current−voltage hysteresis in $CH_3NH_3PbX_3$ perovskite solar cells. *Nat. Commun.* **2016**, *7*, 10334.

(33) Azpiroz, J. M.; Mosconi, E.; Bisquert, J.; De Angelis, F. Defect migration in methylammonium lead iodide and its role in perovskite solar cell operation. *Energy Environ. Sci.* **2015**, *8*, 2118−2127.

(34) Barboni, D.; De Souza, R. A. The thermodynamics and kinetics of iodine vacancies in the hybrid perovskite methylammonium lead iodide. *Energy Environ. Sci.* **2018**, *11*, 3266−3274.

(35) Senocrate, A.; Moudrakovski, I.; Kim, G. Y.; Yang, T.-Y.; Gregori, G.; Grätzel, M.; Maier, J. The Nature of Ion Conduction in Methylammonium Lead Iodide: A Multimethod Approach. *Angew. Chem., Int. Ed.* **2017**, *56*, 7755−7759.

(36) Ferdani, D. W.; Pering, S. R.; Ghosh, D.; Kubiak, P.; Walker, A. B.; Lewis, S. E.; Johnson, A. L.; Baker, P. J.; Islam, M. S.; Cameron, P. J. Partial cation substitution reduces iodide ion transport in lead iodide perovskite solar cells. *Energy Environ. Sci.* **2019**, *12*, 2264−2272.

(37) Travis, W.; Glover, E. N. K.; Bronstein, H.; Scanlon, D. O.; Palgrave, R. G. On the application of the tolerance factor to inorganic and hybrid halide perovskites: a revised system. *Chem. Sci.* **2016**, *7*, 4548−4556.

(38) Lu, J.; Jiang, L.; Li, W.; Li, F.; Pai, N. K.; Scully, A. D.; Tsai, C.-M.; Bach, U.; Simonov, A. N.; Cheng, Y.-B.; Spiccia, L. Diammonium and Monoammonium Mixed-Organic-Cation Perovskites for High Performance Solar Cells with Improved Stability. *Adv. Energy Mater.* **2017**, *7*, 1700444.

(39) Ke, W.; Stoumpos, C. C.; Zhu, M.; Mao, L.; Spanopoulos, I.; Liu, J.; Kontsevoi, O. Y.; Chen, M.; Sarma, D.; Zhang, Y.; Wasielewski, M. R.; Kanatzidis, M. G. Enhanced photovoltaic performance and stability with a new type of hollow 3D perovskite {en}$FASnI_3$. *Sci. Adv.* **2017**, *3*, No. e1701293.

(40) Yokota, I. On the Theory of Mixed Conduction with Special Reference to Conduction in Silver Sulfide Group Semiconductors. *J. Phys. Soc. Jpn.* **1961**, *16*, 2213−2223.

(41) Wagner, C. Galvanische Zellen mit festen Elektrolyten mit gemischter Stromleitung. *Z. Elektrochem., Ber. Bunsenges. physik. Chem.* **1956**, *60*, 4−7.

(42) Maier, J. Complex oxides: high temperature defect chemistry vs. low temperature defect chemistry. *Phys. Chem. Chem. Phys.* **2003**, *5*, 2164−2173.

(43) Maier, J., *Physical Chemistry of Ionic Materials*; John Wiley & Sons, Ltd, 2004; pp 108−480.

(44) Shrestha, S.; Matt, G. J.; Osvet, A.; Niesner, D.; Hock, R.; Brabec, C. J. Assessing Temperature Dependence of Drift Mobility in Methylammonium Lead Iodide Perovskite Single Crystals. *J. Phys. Chem. C* **2018**, *122*, 5935−5939.

(45) Senocrate, A.; Kim, G. Y.; Grätzel, M.; Maier, J. Thermochemical Stability of Hybrid Halide Perovskites. *ACS Energy Lett.* **2019**, *4*, 2859−2870.

(46) Senocrate, A.; Maier, J. Solid-State Ionics of Hybrid Halide Perovskites. *J. Am. Chem. Soc.* **2019**, *141*, 8382−8396.

(47) Kim, G. Y.; Senocrate, A.; Yang, T.-Y.; Gregori, G.; Grätzel, M.; Maier, J. Large tunable photoeffect on ion conduction in halide perovskites and implications for photodecomposition. *Nat. Mater.* **2018**, *17*, 445−449.

(48) Merkle, R.; Maier, J. How Is Oxygen Incorporated into Oxides? A Comprehensive Kinetic Study of a Simple Solid-State Reaction with $SrTiO_3$ as a Model Material. *Angew. Chem., Int. Ed.* **2008**, *47*, 3874−3894.

(49) Denk, I.; Münch, W.; Maier, J. Partial Conductivities in $SrTiO_3$: Bulk Polarization Experiments, Oxygen Concentration Cell Measurements, and Defect-Chemical Modeling. *J. Am. Ceram. Soc.* **1995**, *78*, 3265−3272.

(50) Zibouche, N.; Islam, M. S. Structure−Electronic Property Relationships of 2D Ruddlesden−Popper Tin- and Lead-based Iodide Perovskites. *ACS Appl. Mater. Interfaces* **2020**, *12*, 15328−15337.

(51) Aziz, A.; Aristidou, N.; Bu, X.; Westbrook, R. J. E.; Haque, S. A.; Islam, M. S. Understanding the Enhanced Stability of Bromide Substitution in Lead Iodide Perovskites. *Chem. Mater.* **2020**, *32*, 400−409.

(52) Aristidou, N.; Eames, C.; Sanchez-Molina, I.; Bu, X.; Kosco, J.; Islam, M. S.; Haque, S. A. Fast oxygen diffusion and iodide defects mediate oxygen-induced degradation of perovskite solar cells. *Nat. Commun.* **2017**, *8*, 15218.

(53) Szemjonov, A.; Galkowski, K.; Anaya, M.; Andaji-Garmaroudi, Z.; Baikie, T. K.; Mackowski, S.; Baikie, I. D.; Stranks, S. D.; Islam, M. S. Impact of Oxygen on the Electronic Structure of Triple-Cation Halide Perovskites. *ACS Mater. Lett.* **2019**, *1*, 506−510.

(54) Kohn, W.; Sham, L. J. Self-Consistent Equations Including Exchange and Correlation Effects. *Phys. Rev.* **1965**, *140*, A1133−A1138.

(55) Giannozzi, P.; Andreussi, O.; Brumme, T.; Bunau, O.; Buongiorno Nardelli, M.; Calandra, M.; Car, R.; Cavazzoni, C.; Ceresoli, D.; Cococcioni, M.; Colonna, N.; Carnimeo, I.; Dal Corso, A.; de Gironcoli, S.; Delugas, P.; DiStasio, R. A.; Ferretti, A.; Floris, A.; Fratesi, G.; Fugallo, G.; Gebauer, R.; Gerstmann, U.; Giustino, F.; Gorni, T.; Jia, J.; Kawamura, M.; Ko, H.-Y.; Kokalj, A.; Küçükbenli, E.; Lazzeri, M.; Marsili, M.; Marzari, N.; Mauri, F.; Nguyen, N. L.; Nguyen, H.-V.; Otero-de-la-Roza, A.; Paulatto, L.; Poncé, S.; Rocca, D.; Sabatini, R.; Santra, B.; Schlipf, M.; Seitsonen, A. P.; Smogunov, A.; Timrov, I.; Thonhauser, T.; Umari, P.; Vast, N.; Wu, X.; Baroni, S. Advanced capabilities for materials modelling with Quantum ESPRESSO. *J. Phys.: Condens. Matter* **2017**, *29*, 465901.

(56) Giannozzi, P.; Baroni, S.; Bonini, N.; Calandra, M.; Car, R.; Cavazzoni, C.; Ceresoli, D.; Chiarotti, G. L.; Cococcioni, M.; Dabo, I.; Dal Corso, A.; de Gironcoli, S.; Fabris, S.; Fratesi, G.; Gebauer, R.; Gerstmann, U.; Gougoussis, C.; Kokalj, A.; Lazzeri, M.; Martin-Samos, L.; Marzari, N.; Mauri, F.; Mazzarello, R.; Paolini, S.; Pasquarello, A.; Paulatto, L.; Sbraccia, C.; Scandolo, S.; Sclauzero, G.; Seitsonen, A. P.; Smogunov, A.; Umari, P.; Wentzcovitch, R. M. QUANTUM ESPRESSO: a modular and open-source software project for quantum simulations of materials. *J. Phys.: Condens. Matter* **2009**, *21*, 395502.

(57) Perdew, J. P.; Burke, K.; Ernzerhof, M. Generalized Gradient Approximation Made Simple. *Phys. Rev. Lett.* **1996**, *77*, 3865−3868.

(58) Perdew, J. P.; Ruzsinszky, A.; Csonka, G. I.; Vydrov, O. A.; Scuseria, G. E.; Constantin, L. A.; Zhou, X.; Burke, K. Restoring the Density-Gradient Expansion for Exchange in Solids and Surfaces. *Phys. Rev. Lett.* **2008**, *100*, 136406.

(59) Grimme, S.; Antony, J.; Ehrlich, S.; Krieg, H. A consistent and accurate ab initio parametrization of density functional dispersion correction (DFT-D) for the 94 elements H-Pu. *J. Chem. Phys.* **2010**, *132*, 154104.

(60) Vanderbilt, D. Soft self-consistent pseudopotentials in a generalized eigenvalue formalism. *Phys. Rev. B: Condens. Matter Mater. Phys.* **1990**, *41*, 7892−7895.

(61) Monkhorst, H. J.; Pack, J. D. Special points for Brillouin-zone integrations. *Phys. Rev. B* **1976**, *13*, 5188−5192.